Efficient High-Frequency Body Coil for High-Field MRI

J.T. Vaughan,[1*] G. Adriany,[1] C.J. Snyder,[1] J. Tian,[1] T. Thiel,[2] L. Bolinger,[3] H. Liu,[4] L. DelaBarre,[1] and K. Ugurbil[1]

The use of body coils is favored for homogeneous excitation, and such coils are often paired with surface coils or arrays for sensitive reception in many MRI applications. While the body coil's physical size and resultant electrical length make this circuit difficult to design for any field strength, recent efforts to build efficient body coils for applications at 3T and above have been especially challenging. To meet this challenge, we developed an efficient new transverse electromagnetic (TEM) body coil and demonstrated its use in human studies at field strengths up to 4T. Head, body, and breast images were acquired within peak power constraints of <8 kW. Bench studies indicate that these body coils are feasible to 8T. RF shimming was used to remove a high-field-related cardiac imaging artifact in these preliminary studies. Magn Reson Med 52: 851–859, 2004. © 2004 Wiley-Liss, Inc.

Key words: high field; body coil; MRI; TEM; body imaging

Whole-body imaging at field strengths up to 4T was investigated by MR system manufacturers in the late 1980s (1,2). However, it was thought that the RF power requirements were too high, and RF penetration was too low for successful body imaging above 100 MHz (3). As with most "first" results, the earliest images acquired at higher fields were not the "best" results. Skepticism about high-field body imaging followed, and persisted for nearly a decade (4). Not until recently have technology, support, and interest coalesced to produce encouraging results at fields higher than 1.5 T. Preliminary body imaging results acquired with 55–60-cm inner diameter (i.d.) birdcage transmit coils together with phased-array receivers indicate that 3T whole-body systems may have a clinical role (5). However, these developments are still in their infancy, and there are remaining problems to be solved and performance parameters to be improved. Commercial 128-MHz body coils are usually paired with 35-kW RF power amplifiers to compensate for increased RF losses to the patient and the coil. This is a significant peak power increase compared to 1.5 T MRI, where 15–20-kW amplifiers are more typical. Accordingly, the scope and scale of image protocols operating within FDA specific absorption rate (SAR) guidelines for 3T are highly constrained compared to those for 1.5T.

[1]Center for MR Research, Department of Radiology, School of Medicine, University of Minnesota, Minneapolis, Minnesota.

[2]Bruker BioSpin MRI, GmbH, Ettlingen, Germany.

[3]Institute for Biodiagnostics, National Research Council Canada, Winnipeg, Canada.

[4]Merck Research Laboratories, Rahway, New Jersey.

*Correspondence to: J.T. Vaughan, Center for Magnetic Resonance Research, 2021 Sixth Street SE, Minneapolis, MN 55455. E-mail: tommy@cmrr.umn.edu

By this trend, body imaging at 4T would be more limited still and would require amplifiers approaching a 50-kW peak. Thus, if the human body provided the only significant loss mechanism for imaging at 3T with coil designs requiring 35 kW of peak RF power, body coils and body imaging above 3T would be improbable. However, if it can be shown that RF coil losses contribute a significant fraction of the total loss, then the use of more efficient coil circuits might lessen the total RF losses and make human imaging feasible at 4T and higher.

BACKGROUND

More than most RF coils, the high-frequency body coil challenges the limits of design and performance. Body coils tuned to 128 MHz (3T) and above are required to operate efficiently and homogeneously at unprecedented full-wavelength dimensions. Current approaches to building body coils make use of shielded birdcage-type structures (6–8). The rung currents of birdcage coils generate a homogeneous field transverse to the cylindrical coils' axes. These rung currents depend on end rings for a "return path" (Fig. 1a). However, end rings can be problematic. The inductance and resonance frequency of birdcage coils are dependent on (and limited by) the dimension of the end rings, which in turn define the diameter of the coil. When the diameter is very large, as is the case for body coils, the axial length of the coil must be sufficiently shortened to achieve resonance at the desired operational frequency. However, significantly reducing the length of the body coil can limit the coil's efficiency and homogeneity over the desired field of view (FOV). End-ring currents generate a B_1 field component coaxial with the B_0 field. The axial "z" component of the end-ring generated field is therefore nonproductive for NMR excitation, and can become a source of ohmic loss to induced conduction currents in the tissue load conductor.

To solve the efficiency, homogeneity, and frequency problems associated with end-ring-dependent birdcage coils, we revisited the transverse electromagnetic (TEM) resonator. The TEM design achieves the birdcage's highly homogeneous, rung-current-generated transverse field without the counterproductive end-ring currents (Fig. 1b). The TEM coil's return path follows the shield rather than the end rings. The inductance and self-resonance of the TEM coil are therefore independent of the diameter of the coil. A TEM coil of a given length can be built to arbitrarily large diameters, without significantly changing the frequency of the coil. The basic TEM design derives from the first NMR coil, the coaxial cavity resonator developed by Purcell et al. (9). Schneider and Dullenkopf (10) used the design to construct a high-resolution probe head. Norbert Krause (7) first developed a TEM-like design for human imaging, and Röschmann (11) and Bridges (12) advanced related structures. Over the fol-
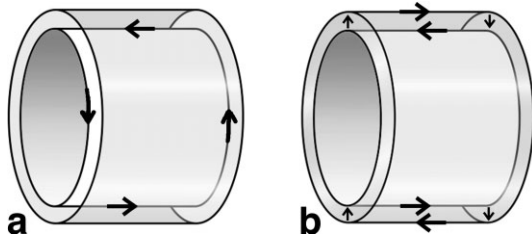
FIG. 1. The resonance of a birdcage coil (**a**) is dependent on and limited by its end rings. Independent of the large, inductive, end-ring circuits, the TEM resonator (**b**) can efficiently achieve the highest frequencies for body coils.

lowing decade the TEM design was improved for modern imaging and spectroscopy applications by Vaughan et al. (13–15). In recent years, a variety of executions have extended the usefulness of the TEM design (16–19).

It is useful to view the segmented TEM volume coil as a toroidal array of independent transmission line elements (Fig. 2). The resonant frequency of the larger TEM coil structure is dependent on the resonant frequency of the independent line element, modified slightly by its reactive coupling with neighboring elements in the coil. The reactance of the individual elements can be tuned in alternating patterns to effect multiple tuning for the larger coil structure (14). The reactance between individual elements can be controlled to decouple the elements for parallel imaging applications (20,26). Any number of individual elements can be driven in transmit and/or receive mode. The individual elements of the volume coil can be actively controlled to tune the coil for transmit, and detune the coil for reception with local receivers, such as surface coils, phased arrays, or parallel arrays (15). The amplitude and phase of the elements can be modulated to effect corrective RF field shimming or volume selection (21). Many such advantages of the segmented TEM body coil are demonstrated in this work.

MATERIALS AND METHODS

Theoretical Models

Calculated Coil Losses

To numerically calculate the operational frequency and efficiency ranges for high-field volume coils, we modeled five unloaded coils by the finite difference time domain (FDTD) method (22) (Fig. 3). The equivalent total capacitance and radiation resistance were calculated vs. the transverse mode resonant frequency for high- and low-pass, shielded and unshielded birdcages, and a TEM resonator. All five coils had identical dimensions (58 cm i.d. × 33 cm long) and were open on both ends. The birdcage shields and the TEM cavity were 1.0 m long and spaced 2 cm from the coil rungs. These models were in their "classic" forms: the low-pass birdcage included 24 capacitors in center positions on the rungs, the high-pass birdcage included 24 capacitors in each ring for a total of 48 in the structure, and the TEM resonator included 48 capacitors in rung positions. Capacitor positions in these models appear as gaps in the circuits of Fig. 3. While the models faithfully reproduce the configuration of the TEM body coil tested, all coil models might be improved with more highly distributed capacitances.

We assigned values to the capacitors shown in Fig. 3 in order to tune the resonant frequencies of the coil models, as in realized coil circuits. To determine the point at which a coil reached self-resonance, we calculated the equivalent added capacitance of the structure vs. the resonant frequency associated with the transverse B_1 field mode for each of the models as shown. The coil approached self-resonance as the equivalent added capacitance approached zero. The results are plotted in Fig. 4a. According to the results displayed in Fig. 4, 1 pF will resonate the low-pass birdcage body coils at slightly higher than 64 MHz (1.5T), with the shielded coil reaching a higher frequency than the unshielded birdcage. High-pass birdcage coils reach 128 MHz (3T) for the same 1-pF capacitance added, again with the shielded version resonating higher. The TEM coil of the same dimensions and capacitance reaches 342 MHz (8T).

To quantify the amount of energy lost to radiated fields, the radiation resistance ($R_r = 2P_r/I_m^2$, where P_r is the radiated power, and I_m is the maximum current in the coil vs. resonant frequency) was calculated for each coil structure and plotted in Fig. 4b (15,23). The model shielded high-pass birdcage body coil resonating at 128 MHz radiates energy to the patient load and the magnet bore at a rate equivalent to the energy lost to a 20-ohm resistor in the coil circuit. By the same model, the TEM coil would incur approximately half this loss at 3T and 4T Larmor frequencies. Because the TEM coil is less radiative and inductive than the birdcage, its useful range as a full-sized human body coil approaches 350 MHz (>8T). This prediction agreed with bench measurements.

Calculated Coil Fields

The 3D Maxwell B_1 field contours for the TEM body coil were calculated by the FDTD method (Fig. 5). The central transaxial field (Fig. 5b) is highly homogeneous and does not vary by >1 db over a 46-cm-diameter FOV. This transaxial homogeneity is typical of birdcage coils as well. To compare the axial field profile of the TEM body coil to birdcage profiles, we calculated the B_1 field contour along the *z*-axis of the models shown in Fig. 3. The relative B_1 magnitudes were normalized to respective peak B_1 fields generated by equal currents on the coil elements. Normalized B_1 field results are
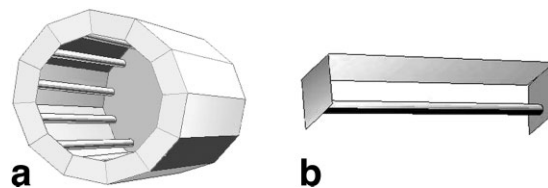

FIG. 2. The segmented TEM volume coil (**a**) can be described as a toroidal array of TEM elements (**b**), formed by current elements parallel to cavity wall or shield sections. These TEM elements are the building blocks of the TEM volume coil. The impedance of the independent RF current elements can be passively or actively controlled for detuning, retuning, multiple tuning, phase shifting, amplitude modulation, transmission, and reception. The elements of the TEM volume coil may be reactively coupled and connected to the system transmitter(s) and or receiver(s) by a subset of the total element number, or may be reactively decoupled and connected at every element.

FIG. 3. Body coil models for FDTD calculations of frequency limits and radiation resistance for shielded and unshielded (not shown) body coils. The coil rung counts and physical dimensions are equal in the shielded low-pass birdcage (**a**), shielded high-pass birdcage (**b**), and TEM (**c**) models, as shown.
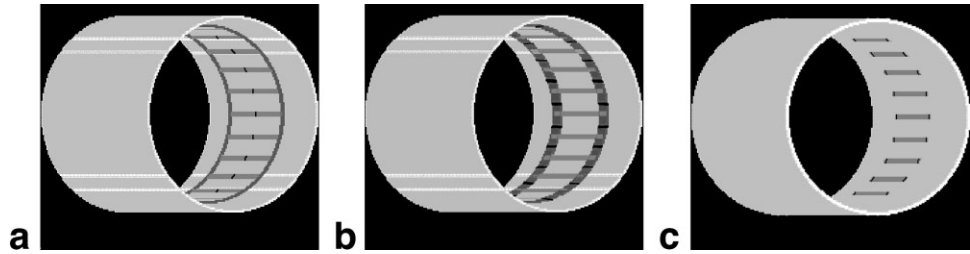
shown in Fig. 6. The three equal-length coils modeled are shown to have differing field lengths (the axial field length of each coil is defined as the points on the $\pm z$-axis at which the B_1 magnitude falls to 3 dB below the peak value reached in the coil center). The unshielded birdcage axial field length of 24.7 cm is comparable to the shielded birdcage field of 32.5 and the TEM axial field length of 35.8 cm.

Calculated Body Losses

Coil losses, whether from conserved or radiated fields in the coil, are mostly spent as RF losses to the tissue conductor and the tissue dielectric in the human body (14). RF field propagation and loss in the body-loaded coil were modeled by the FDTD method (Fig. 7). In these models, anatomic boundaries were assigned frequency-dependent permittivity and conductivity values (24). The current density, A/m², was calculated for a uniform transverse, circularly polarized field generated by the body coil at 128 MHz. The relative distribution of the current density is shown in Fig. 7a, color-coded for one order of magnitude (red is 10-fold greater than blue). Note the sharp current density gradient through the heart and in the chest walls. Regions of high-current-density gradients correlate to regions of B_1 nonuniformity. The relative RMS power loss density, W/m³, across the chest is shown in Fig. 7b (red is 10-fold greater than blue). As might be expected, the greatest losses occur in the regions of highest current density in the load. These models predict a quadratic increase in average power vs. frequency.

Design and Construction

Body Coil Structure

The body coil designed and built for this study followed that of the actively detunable TEM volume coil (15,25,26). As shown in Fig. 8a, the supporting member of the coil

was a 5-mm-thick, 100-cm-long fiberglass cylinder with an outside diameter (o.d.) of 62 cm. While the element centers were at 58 cm i.d. as modeled, the coil package i.d. was 56 cm. For maximum eddy-current-free shielding between the gradients and the RF coil, a double-sided, copper foil-clad, polyimide film (Sheldahl, Inc.) was laminated to the full-length i.d. of the cylinder. The copper foil was segmented as shown in Fig. 8b, with the inside and outside foil layers overlapping. Each foil segment was centered with and parallel to a connecting coil "rung" or current element positioned in the central third (33 cm) of the coil. Coaxial elements were used in this study, and each element center was spaced 2 cm away from the segmented shield (15,20). A more compact means of constructing current elements was achieved by etching the elements on a flexible circuit board material, as shown in Fig. 8c. Tuning capacitance was added to the elements by etching overlapping layers on a double-sided board. However, all components of the TEM elements, including the distributed circuits, lumped-element circuits, coaxial lines, flat lines, strip lines, microstrips, waveguides, and cavities are options (14,15,20).

Body Coil Control

The elements of the active coil section were driven in quadrature at four positions, and actively tuned and detuned for independent transmit and receive operations at every element (Fig. 9). Actively controlled PIN diode circuits (MA4Pk2002, M/A-COM) tuned and detuned the body coil for transmit and array receive functions, respectively. The body coil was reactively tuned to 170 MHz. The impedance of the RF current elements in the TEM coil was independently adjusted to optimize or "shim" a region of interest (ROI). The RF field was interactively shimmed over an anatomic region by adjusting tuning stubs to control element impedance (phase and amplitude) in response
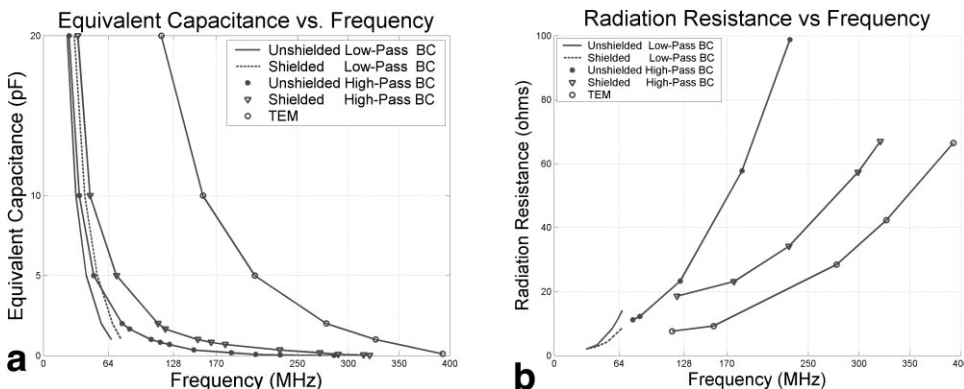

FIG. 4. In the FDTD calculations for the Fig. 3 coil structures, self-resonance (**a**) and radiation losses (**b**) are shown to limit the use of birdcage body coils to approximately $\leq$3T (128 MHz), whereas the TEM body coil may be useful to 8T. The plots for the low-pass body coils in **b** are limited by the maximum resonance frequencies of these coils.
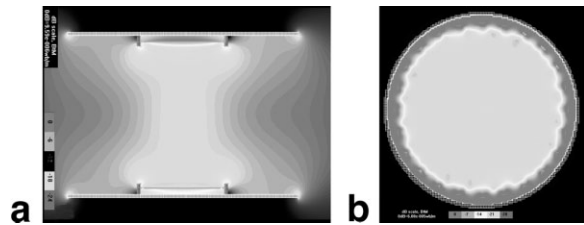
FIG. 5. B_1 field contours (1 dB) were calculated in the axial (**a**) and transaxial (**b**) planes by the FDTD method for the unloaded, quadrature-driven body coil. **a:** The 33-cm coil elements (rungs) are shown in the central third of the 1-m-long cavity for the coil.

to image signal feedback. We are currently refining this mechanical control mechanism for adjusting element impedance to achieve algorithm-driven electronic control with negative feedback.

Body Coil System

An active body coil system was developed for efficient head and body imaging at field strengths of 3T and higher (Fig. 10). This complete RF front-end system employed the actively detuned TEM body coil for NMR signal excitation together with phased- and parallel-array local receiver coils. Not shown are the high-power, nonmagnetic transmit/receive (TR) switches that completed the RF front end (27).

RESULTS

Bench Measurements

The 56-cm-i.d. TEM body coil was tuned and evaluated at 128 MHz (3T), 170 MHz (4T), and 347 MHz (8T+) on the electronics test bench. A network analyzer was used to measure the S11 reflection and S12 transmission characteristics for each coil. The S11 spectra shown (Fig. 11) demonstrate that each body coil was easily tuned and well matched at the respective operational frequencies indicated. The characteristic transverse field mode for N runged TEM coils is the second lowest in a spectral field of $N/2 + 1$ resonant modes for the coil (14). We determined the relative coil circuit efficiency by measuring Q ratios and B_1 gains. Tuned and matched to 128 MHz, the Q ratio of the unloaded coil to the 75-kg subject-loaded coil was $Q_u/Q_l = 740/50$, and at 170 MHz the ratio was 720/40. The Q measurements for a coil at 344 MHz were $Q_u/Q_l = 520/30$. The high Q values for the unloaded TEM body coil can be observed as the narrow line widths of the S_{11} spectra in Fig. 11. The lines are too narrow to show the full −50 dB impedance match conditions reached, by the resolution allowed by the full spectral bandwidth of the S_{11} plots. The relative B_1 gain of each coil was determined by the S_{12} measurement, which we obtained by driving the body coil with a calibrated transmit power input and receiving the B_1 field generated with a calibrated field probe placed in the center of the body coil, and aligned with the field for maximum signal. It should be noted that the B_1 gain was preserved for the TEM body coil, from 128 MHz (3T) to at least 342 MHz (8T). Also notable is the fact that B_1 field contributions from resonances adjacent to the transverse field mode are negligible. According to these

network measurements, the full-sized TEM body coil is efficient and well behaved to 8T.

In Vivo Results

Successful in vivo results have been obtained from six TEM body coils tested at 3T, 4T, and 4.7T. The results in this paper were acquired with the body coil described and two industrial 4T systems. Figs. 12b, 13a,c,d, 14 and Table 1 were acquired with a Varian Inova console, Oxford magnet, and Siemens Sonata gradients, with 1-kW and 8-kW RF power amplifiers from American Microwave Technologies (AMT) and Communications Power Corporation (CPC), respectively. Figs. 12a and 13b were acquired on a Bruker MedSpec 4T MRI system interfaced to an Oxford magnet, Siemens Sonata gradients, and a Dressler 4-kW RF power amplifier. The Bruker system did not make use of the front-end components listed in Fig. 10.

Body Coil Efficiency

On the Varian system, we used 90° flip angle calibration measurements to quantify coil efficiency with respect to a given load. From the human abdomen, 90° flip angle measurements were acquired from transaxial slices by the image signal intensity projection method (30). An equivalent 1-kW, 1.7-ms square pulse was required to achieve a 90° calibrated slice through the abdomen of a 95-kg male subject (Fig. 13a). A 1-kW, 1-ms square pulse was required for a 55-kg female subject. The body imaging conducted in this study was limited by the lack of an adequately rated power amplifier, the high cost and limited availability of which provided some motivation for the current research. Therefore, all of the images acquired in this study were obtained with low peak power sequences. Nevertheless, the results were promising and the efficiency with which these images were acquired generally exceeded previously published predictions for 4T body imaging (3). Extrapolating from these 90° measurements on the Varian system, a 15-kW power amplifier should be sufficient to excite 180° flip angles in large patients by means of a 1-ms square
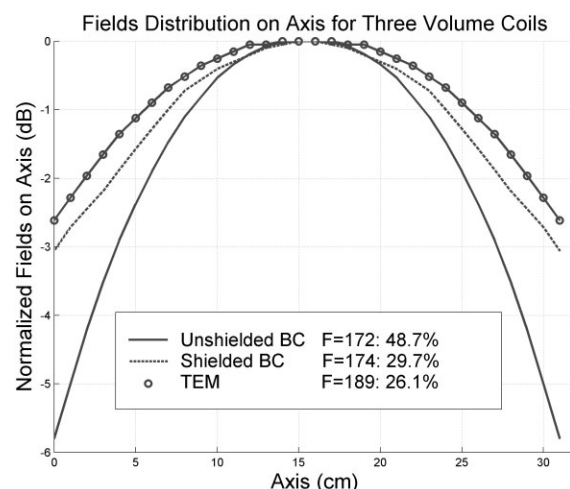

FIG. 6. The normalized B_1 field magnitude generated along the z-axis of the Fig. 3 models is shown. The coil elements or rungs for the birdcages and the TEM resonator are 33 cm long.

Current Density

Power Loss Density

FIG. 7. Induced RF currents and losses were calculated by the FDTD method for the human body. The steepest current density gradients and resultant losses are seen in the peripheral regions of the body closest to the coil, and in the heart (courtesy of W. Renz, Siemens Medical Solutions, Erlangen, Germany).
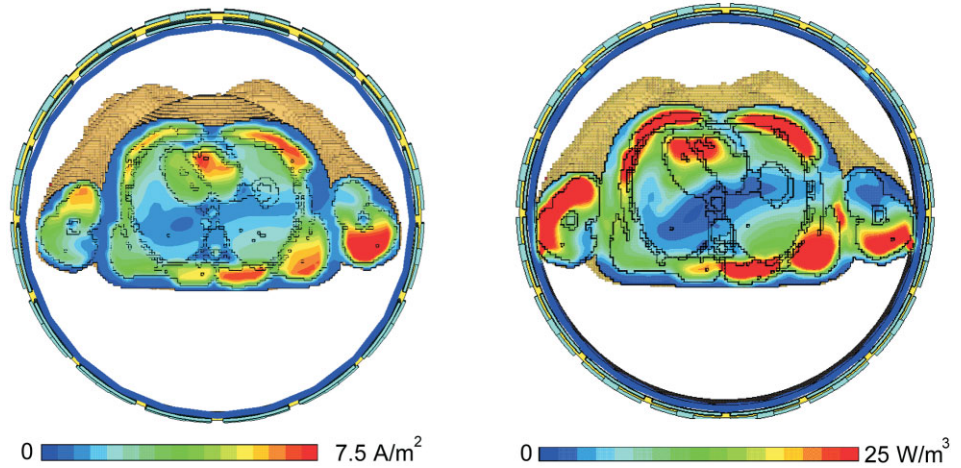
pulse. A separate but similar RF power requirement study was conducted on the Bruker 4T system, with somewhat more promising results. These results are tabulated in Table 1 for three patient sizes and three body locations (i.e., the head, thorax, and abdomen).

Body Coil FOV

The axial FOV for the TEM body coil is dependent on its current element lengths, which are in turn decided by the gradient coil length and performance. In agreement with the models shown in Figs. 5 and 6, the 58-cm i.d. test coil with 33-cm current elements was measured to have a field uniformity of ± 1.5 dB over a cylindrical volume (36 cm long, 46 cm in diameter). Ten centimeters outward from each end of the 33-cm element cylinder, the B_1 field magnitude dropped by 7 dB on the axis. This relatively steep B_1 field decline off the ends of the coil elements minimized image "wrapping" due to RF signal contributions from beyond the gradient coil's axial performance limit. This rapid RF gradient at the edge of the body coil is evident in the image signal cutoff at the base of the neck in Fig. 12a. Also, in contrast to previous results (2–4,31), the images of Fig. 13a and b from multislice data sets demon-

strate surprising RF penetration and uniformity through the trunk of a relatively large (95-kg) subject at 4T.

Body Coil Applications

We selected four regions of the body (the head, chest, abdomen, and breast) to demonstrate the feasibility of whole-body imaging at 4T. The images in Figs. 13c and d, and 14 were all acquired with the use of a TEM body coil for homogeneous excitation, and phased- or parallel-array receivers. The head image in Fig. 12b was acquired with a four-loop, strip-line, parallel-array receiver from which image components were combined by a simple magnitude addition (32). The homogeneous transmit field constructively interfering in the center of the head combined with the array elements' reception bias toward the periphery of the head results in a more uniform image compared to these from trasmit-receive head coils. The abdomen image in Fig. 13c was acquired with a four-channel, phased-array receiver using a breath-held, T_1-weighted, recalled-echo sequence. Each loop of the phased-array receiver pairs measured 14 cm $\times$ 19 cm, with the 19-cm legs overlapped to achieve critical decoupling between the loops. One pair of loops was placed on top of the abdomen of the supine
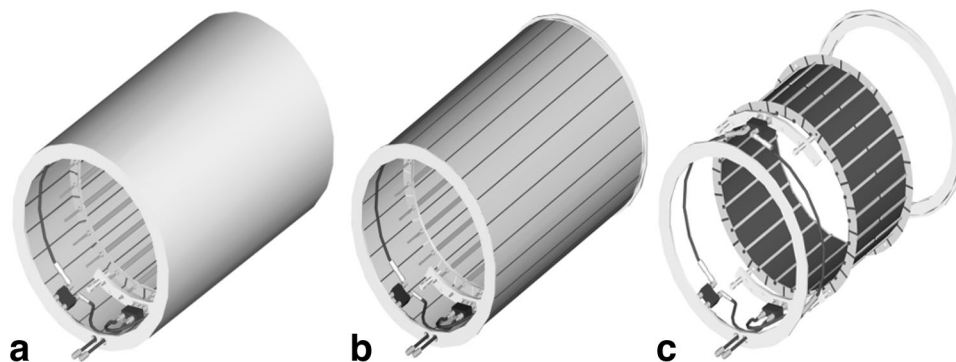

FIG. 8. The plan for the TEM body coil is shown (25). **a:** The freestanding, packaged body coil without the inner liner. **b:** The supporting fiberglass cylinder is removed to reveal the slotted TEM cavity wall. Inside and connected to the cavity wall are the current elements shown in **c**. A network of two 180° hybrids and two 90° quadrature hybrids with cabling is shown driving the coil at four elements 90° apart. The transmit and receive cables for the coil structure are seen projecting from the bottom of the coils (15). See also Fig. 9.
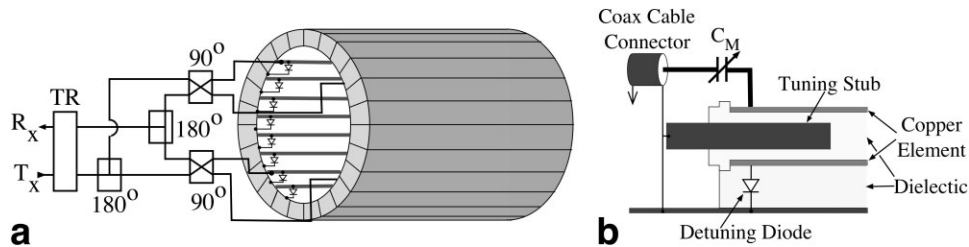
FIG. 9. **a:** The actively detunable TEM body coil is shown with a four-port quadrature drive circuit and TR switch interfacing the coil to the RF transmitter and receiver paths of the MR system. Part **b** shows how the cable is connected to a driven element, and how this element is tuned via the stub and detuned by the actively switched diode.

subject, and the other pair was placed beneath the abdomen. The vertical line artifact in the uncorrected image is due to pulsatile motion in the descending aorta. The high-resolution, T_1-weighted, spin-echo breast image in Fig. 13d was acquired with quadrature crossed-pair phased arrays. Figure 14 shows a pair of breath-held, gradient-echo cardiac images acquired with EKG gating from a 73-kg male. The four-loop phased array described above for the abdomen imaging was also used for the cardiac imaging, with two loop pairs being centered anterior and posterior to the heart on a supine volunteer. Note the RF artifact observed as a signal dropout in the right atrium of the image in Fig. 14a. This artifact appeared consistently in all of the four subjects imaged. The cause of this artifact is prominently featured as a significant RF current density gradient in Maxwell models of the human chest at 128 MHz (Fig. 7a). In the 4T experiment, this artifact was consistently and quickly removed by a small number of iterative adjustments of the magnitude and phase of the body coil's RF field, by means of an RF field shimming technique (21) (Fig. 14b).

DISCUSSION

Body Coil

Theory predicts that the TEM design is an efficient candidate for a high-frequency body coil. Efficiency increases with lower radiation resistance compared to high-pass birdcage designs of equal size, as shown in Fig. 4b. The absence of significant end-ring-generated fields, and the

shorter coil circuit requirements for a given FOV also increase the efficiency of the TEM body coil. High unloaded Q values (Fig. 11) and efficient RF power usage (Table 1) support the theory. Because the TEM coil is essentially a cylindrical array of independent resonant elements, it is less inductive than an end-ring-dependent birdcage coil of equal size and element count. Therefore, the TEM coil can be built to larger dimensions and still achieve very high frequencies, as predicted (Fig. 4a) and measured on the bench (Fig. 11). According to Fig. 6, the axial field of the TEM body coil extends somewhat further than that of a shielded birdcage of the same physical size. This difference between the axial field profiles of two coils is probably due to the respective presence or absence of significant end-ring currents in the two designs (the end-ring field of the birdcage being nonproductive for NMR signal generation, and a likely source of loss). A shorter and thus more efficient TEM coil could approximate the axial field profile of a longer birdcage for faster cutoff at the edge of the useful B_0 field gradients. Because the Faraday shield is integral to the coil circuit, the TEM body coil is conveniently tuned at the bench during a one-time setup procedure, and is then inserted into the magnet bore with no further adjustment required. This feature makes the coil portable and easily installed in the field. It can be inserted or removed from the magnet as needed. The standard high-pass, shielded birdcage can be improved by increased amounts of distributed capacitance, and this prototypical TEM coil can be similarly refined. Equivalent models of both designs were compared in the calculations.
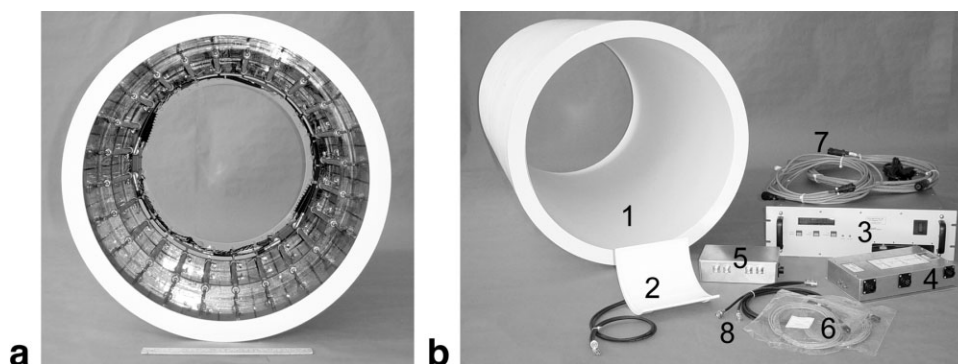

FIG. 10. The constructed TEM body coil is shown together with the complementary front-end equipment required for implementation and application of the active body coil and multichannel receiver system. Included in the system are a homogeneous transmit coil (1); multichannel receiver coil (2); coil power supply and control unit (3); optically triggered, nonmagnetic PIN diode driver unit (4); nonmagnetic, multichannel preamplifier (5); and all of the necessary fiber optic control lines (6), power supply lines (7), and RF signal cables (8).
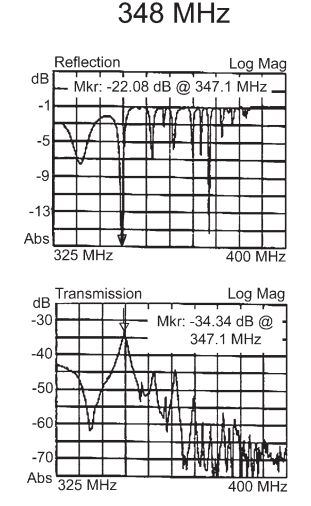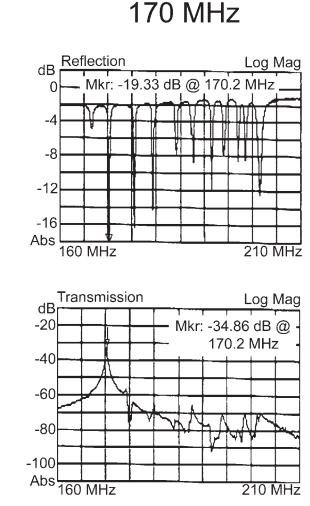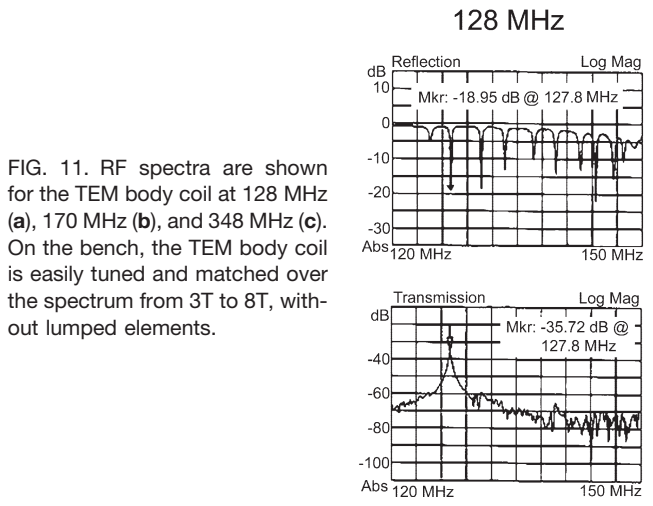
128 MHz 170 MHz 348 MHz

FIG. 11. RF spectra are shown for the TEM body coil at 128 MHz (**a**), 170 MHz (**b**), and 348 MHz (**c**). On the bench, the TEM body coil is easily tuned and matched over the spectrum from 3T to 8T, without lumped elements.

Magnet bore space for a body coil is often limited. To reduce the approximately 2.5-cm coil profile (o.d.–i.d.)/2, one can replace the air dielectric with Teflon or other dielectric materials to achieve closer element-to-foil physical spacing for efficient electrical (wavelength) spacing. Alternatively, the space between the elements and the shield might be used for acoustic dampening materials, for conductive or dielectric elements for B1 field shaping or for B0 shims. One can also select the distance and dielectric materials between the current elements and the shield to control the mutual coupling or decoupling between the TEM elements (15,26). For example, when the current elements are spaced approximately 2 cm or more away from the shield, the TEM resonator can be homogeneously excited by and received from only four reactive elements in the coil (15, 28). The remaining elements in the TEM resonator are coupled by mutual induction. However, as the current elements are brought closer to the shield sections, inductive coupling to neighboring elements decreases to a point where the TEM elements become substantially decoupled. When all of the elements are mutually decoupled, they must be independently coupled directly to transmit and/or receive circuits. The resulting array of decoupled TEM elements has been demonstrated
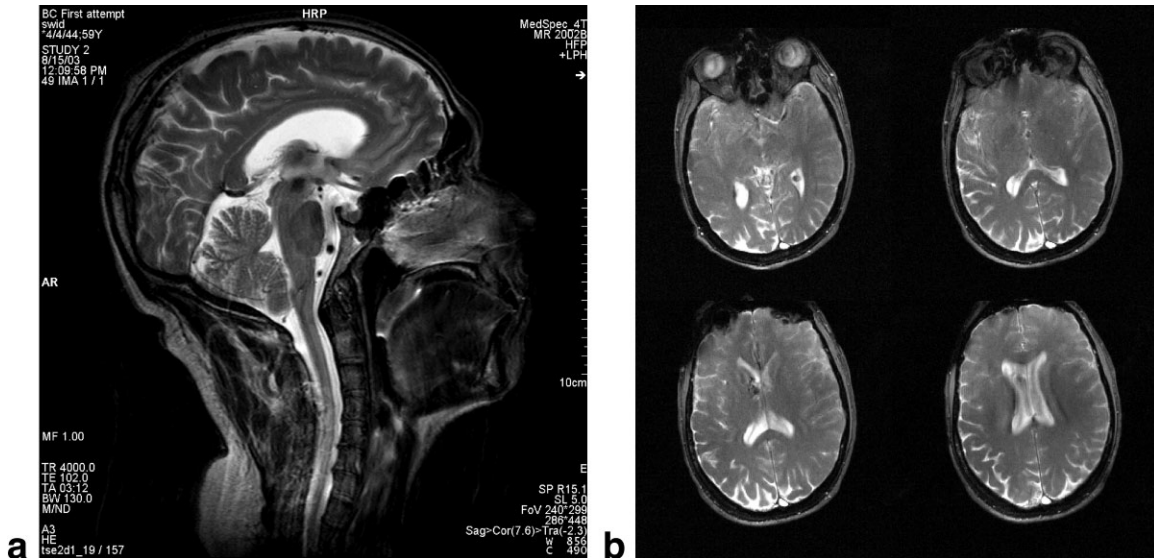
FIG. 12. **a:** One of a sagittal multislice set of turbo spin-echo head images acquired with the TEM body coil only (acquisition parameters: TR = 4000 ms, TE = 102 ms, slice = 5 mm, FOV = 299 × 240 mm, matrix = 448 × 286, NEX = 3, acquisition time = 3:12, bandwidth = 130 Hz/px, refocusing flip angle = 157°). Image acquired on a Bruker MedSpec 4T system with RF power limited to a ~3-kW peak. **b:** Four images from a multislice set of 4T brain images acquired with a TEM body coil transmitter and a four-loop, parallel-array receiver. The receiver coil was composed of four loops (13 cm × 13 cm) evenly spaced 4 cm apart on a 22-cm-diameter cylinder. This "brain band" was worn on the cranium. The acquisition parameters for this multislice gradient-echo sequence were TR = 9.5 ms, TE = 1 s, slice = 5 mm, FOV = 22 cm^2, matrix = 256 × 128. Images from individual, receive only array loops were combined without intensity correction. The characteristically bright image center due to constructive interference of RF fields in transmit-receive head coils at 4T, is compensated here where the transmit field bias toward the center of the head is balanced by the receiver array sensitivity to the periphery. A 1-kW RF power amplifier was used to acquire this image set on a Varian Inova 4T system.
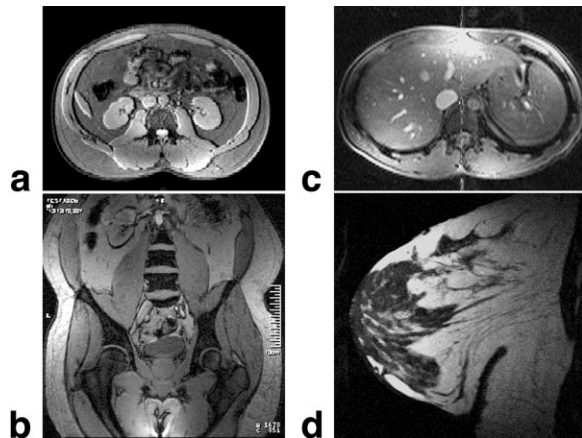
FIG. 13. **a** and **b:** Transmit and receive images acquired with a 4% body coil only. **c** and **d:** Images acquired with the 4T body coil for homogeneous excitation together with phased arrays for local reception. Specifically, image **a** is one slice of a multislice, interleaved, gradient-echo transverse body image set acquired from a 95-kg male on a Varian 4T system. Acquisition parameters for this data set were TR = 250 ms, TE = 5.2 ms, slice = 5 mm, slice gap = 10 mm, FOV = 48 × 36 cm, matrix = 256 × 128, NEX = 2. The SAR was 1.35 W/kg for the 10-slice acquisition, and 800 W peak RF power was used for low tip pulse. **b:** A multislice set of 3-mm-thick images shows strong homogeneity and signal for a 95-kg subject, with RF peak power limited to approximately 3 kW on a Bruker 4T system. This single slice of 16, breath-held, interleaved, multislice T_1 FLASH images was acquired with the body coil only (TR = 96 ms, TE = 5.2 ms, slice = 3 mm, matrix = 320 × 256, flip angle = 70°, bandwidth = 180 Hz/px, scan time =16 s). **c:** One image from a multislice set of 4T abdominal images acquired with the TEM body coil transmitter and phased-array receivers. Simple magnitude addition was used to combine the array received images without intensity correction. The inhomogeneities observed are characteristic of the receiver arrays used. Images were acquired with a four-channel, phased-array receiver using a breath-held, recalled-echo sequence (TR = 200 ms, TE = 3.9 ms, flip angle = 90°, slice = 5 mm, FOV = 36 × 27 cm, matrix = 256 × 96). An 8-kW RF power amplifier was used for this acquisition on a Varian system. **d:** One of 16 4T breast images acquired with a TEM body coil transmitter and a phased-array receiver. High-resolution, T_1-weighted, spin-echo breast images were acquired with quadrature crossed-pair phased arrays (TR = 400 ms, TE = 21 ms, slice = 3 mm, slice gap = 1 mm, FOV = 20 cm², matrix = 512 × 512, NEX = 2). Two 16-cm loops formed each pair of the dual breast coil in position beneath a prone woman, within the body coil. No intensity correction or image processing was applied.

to be useful for parallel imaging applications (29). The independent TEM elements can also be controlled by active or passive means to affect a variety of functions to support anatomic, multinuclear, and functional imaging. These control functions at the elemental level include transmitting and receiving, switching, tuning and detuning, multiple tuning, mutual decoupling, phase shifting, and amplitude modulation (26). The TEM volume coil should be considered for all available superconducting magnets, including the new 9.4T human bore magnets recently installed at the University of Minnesota and at the University of Illinois–Chicago.

Body Coil Images

At the time this study was conducted, whole-body imaging was limited by low RF power levels, long pulse widths,
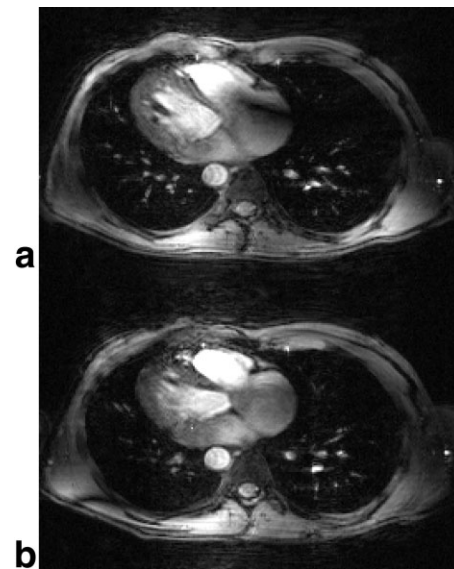
FIG. 14. Preliminary 4T gated cardiac images were acquired with the TEM body coil transmitter and phased-array receivers. An artifact in the right atrium common to 4T heart images (**a**) is corrected by RF shimming (**b**). Images were acquired with a four-channel, phased-array receiver using an EKG gated gradient-echo sequence (TE = 4.3 ms, slice = 5 mm, FOV = 40 × 30 cm², matrix = 256 × 128). An 8-kW RF power amplifier was used to drive the transmit coil. No intensity correction was applied to these four-loop, phased-array images.

and sometimes low flip angles necessitated by the available RF power amplifiers. Consequently, we were unable to perform many standard protocols requiring full inversions on the human trunk. The use of spin-echo images, which are more B_1-sensitive, would have better addressed questions about RF homogeneity and SAR limits for body imaging at 4T. However, the spin-echo images of the head and breast did show good homogeneity and SNR (Figs. 12a and 13d). Working within the RF power limitations, we obtained preliminary extrapolations of the RF power requirements for 4T whole-body imaging (Table 1). An RF power amplifier of 15 kW will meet many imaging requirements with the TEM body coil at 4T. The fact that the SAR is linearly proportional to the number of slices, and inversely proportional to TR is expected to limit the number of slices at 4T compared to lower field strengths for power-aggressive protocols. However, the multislice images acquired for this study with the TEM body coil were well within FDA guidelines (Figs. 12–14). Relatively uniform

Table 1
RF Power Requirements for Whole Body Imaging at 4T

1 ms inversion block pulse	Weight, kg	kW	Angle
Abdomen = 10.9 kW for 95kg human	60	3.1	120
	75	3.1	114
	95	3.0	96
Thorax = 6.7 kW for 95kg human	60	3.1	150
	75	3.1	135
	95	3.0	120
Head = 5.4 kW for 95kg human	60	3.1	178
	75	3.1	169
	95	3.0	139

RF penetration was also measured over a range of body sizes. Where a B1 artifact did arise in the heart, a novel solution (termed "B_1 shimming") was advanced to correct it (Fig. 14). B_0 shimming is somewhat more difficult at 4T compared to lower fields, but is performed similarly with good results. Auto-shimming was implemented with higher shim currents. When the array coils were used, they facilitated shimming as well. Coil eddy currents were not problematic, indicating there was an effectively slotted RF cavity on the body coil. For the pulse sequences employed, ghosting was <1% of the image signal. If eddy currents are a problem, the foil cavity can be segmented further. Some whole-body images acquired with the body coil showed a chemical shift artifact due to the extremely low pulse peak and long pulse width used (Fig. 13a). In Fig. 13c, contrast is lacking and mottled as a result of unoptimized parameters, a high flip angle, and a relatively short TR. With more power, good T_1 contrast could be achieved at 4T with MDEFT and similar sequences (33). The signal intensity variation and flow artifact from the descending aorta in Fig. 13c are characteristic of uncorrected phased-array receivers and uncompensated, raw image data. To ensure that any coil and high-field-related B_1 field effects would be revealed, the images were not intensity-corrected or otherwise processed. While the images shown are preliminary and not yet of diagnostic quality, they are unprecedented for 4T and support the feasibility of 4T whole-body imaging.

CONCLUSIONS

An efficient, self-shielded, actively detuned TEM body coil is described in this study. The initial bench measurements and in vivo results support the TEM body coil's potential utility with the range of magnets currently available for human studies at 3–8T or higher. MRI of the whole human body is feasible at 4T. These initial results will improve with further refinements to the technique and technology used, especially with more peak RF power. The images presented suggest that with an efficient and dynamically adjustable body coil, RF power requirements and field penetration need not be barriers to clinical body imaging at 4T.

REFERENCES

1. Barfuss H, Fischer H, Hentschel D, Ladebeck R, Vetter J. Whole-body MR imaging and spectroscopy with a 4-Tesla system. Radiology 1988; 169:811–816.
2. Bomsdorf H, Helzel T, Kunz D, Roschmann P, Tschendel O, Wieland J. Spectroscopy and imaging with a 4 tesla whole-body MR system. NMR Biomed 1988;1:151.
3. Röschmann PK. Radiofrequency penetration and absorption in the human body: limitations to high-field whole-body nuclear magnetic resonance imaging. Med Phys 1987;14:922–931.
4. Wen H, Denison TJ, Singerman RW, Balaban RS. The intrinsic signal-to-noise ratio in human cardiac imaging at 1.5, 3, and 4 T. J Magn Reson 1997;125:65–71.
5. Watkins RD, Rohling KW, Piel J, Rosenfeld D, Kelley D, Lenkinski R, Kressel H, Montag A. Whole body RF coil for 3 Tesla MRI system. In: Proceedings of the 9th Annual Meeting of ISMRM, Glasgow, Scotland, 2001. p 1123.
6. Alderman DW, Grant DM. An efficient decoupler coil design which reduces heating in conductive samples in superconducting spectrometers. J Magn Reson 1979;36:447–451.
7. Krause N. Siemens Aktiengesellschaft, Munich, assignee. High frequency field system for nuclear magnetic resonance apparatus. U.S. patent 4,506,224; 1985.
8. Hayes CE, Edelstein WA, Schenck JF, Mueller OM, Eash M. An efficient highly homogeneous radiofrequency coil for whole-body NMR imaging at 1.5T. J Magn Reson 1985;63:622–628.
9. Purcell EM, Torrey HC, Pound RV. Resonance absorption by nuclear magnetic moments in a solid. Phys Rev 1946;69:37.
10. Schneider HJ, Dullenkopf P. Slotted tube resonator: a new NMR probe head at high observing frequencies. Rev Sci Instrum 1977;48:68.
11. Röschmann PK. High-frequency coil system for a magnetic resonance imaging apparatus. U.S. patent 4,746,866; 1988.
12. Bridges JF. Cavity resonator with improved magnetic field uniformity for high frequency operation and reduced dielectric heating in NMR imaging devices. U.S. patent 4,751,464; 1988.
13. Vaughan JT, Hetherington HP, Harrison JG, Otu JO, Pan JW, Noa P, Pohost GM. High frequency coils for clinical nuclear magnetic resonance imaging and spectroscopy. Phys Med 1993;IX:147–153.
14. Vaughan JT, Hetherington HP, Otu JO, Pan JW, Pohost GM. High frequency volume coils for clinical NMR imaging and spectroscopy. Magn Reson Med 1994;32:206–218.
15. Vaughan JT, Adriany G, Garwood M, Yacoub E, Duong T, DelaBarre L, Andersen P, Ugurbil K. A detunable transverse electromagnetic (TEM) volume coil for high field NMR. Magn Reson Med 2002;47:990–1000.
16. Baertlein B, Ozbay O, Ibrahim T, Lee R, Yu Y, Kangarlu A, Robitaille P. Theoretical model for an MRI radio frequency resonator. IEEE Trans Biomed Eng 2000;47:535–545.
17. Zhang X, Ugurbil K, Chen W. A microstrip transmission line volume coil for human head MR imaging at 4T. J Magn Reson 2003;161:242–251.
18. Beck B, Plant D, Grant S, Thelwall P, Silver X, Mareci T, Benveniste H, Smith M, Collins C, Crozier S. Progress in high field MRI at the University of Florida. MAGMA 2002;13:152–157.
19. Bogdanov G, Ludwig R. Coupled microstrip line transverse electromagnetic resonator model for high-field magnetic resonance imaging. Magn Reson Med 2002;47:579–593.
20. Vaughan JT. An improved volume coil for high field MRI. In: Proceedings of the 7th Annual Meeting of ISMRM, Philadelphia, 1999. p 167.
21. Vaughan J, Snyder C, Adriany G, Bolinger L, Liu H, Stolpen A, Ugurbil K. The technology and techniques of 4T body imaging. In: Proceedings of the 11th Annual Meeting of ISMRM, Toronto, Canada, 2003. p 425.
22. Kunz K, Luebbers R. The finite difference time domain method for electromagnetics. Boca Raton, FL: CRC Press; 1993.
23. Tian J, Vaughan J. Frequency limits and radiation resistance for volume coils. In: Proceedings of the 11th Annual Meeting of ISMRM, Toronto, Canada, 2003. p 2354.
24. Duck F. Physical properties of tissue. London: Academic Press; 1990.
25. Vaughan JT, Adriany G, Bolinger L, Waks M, DelaBarre L, Garwood M, Andersen P, Ugurbil K. A body coil for high field MR. In: Proceedings of the 10th Annual Meeting of ISMRM, Honolulu, 2002. p 160.
26. Vaughan JT. RF coil for imaging system. U.S. patent 6,633,161; 2003.
27. Vaughan JT, Haupt DN, Noa PJ, Pohost GM. RF front end for a 4.1 tesla clinical spectrometer. IEEE Trans Nucl Sci 1995;42:1333–1337.
28. Zhang N, Roos MS, Vaughan JT, Wong STS, Budinger TF. Head coil B1 field inhomogeneity and SNR performance at 8–10T. In: Proceedings of the 4th Annual Meeting of ISMRM, New York, 1996. p 252.
29. Boskamp E, Lee R. Whole body LPSA transceive array with optimized transmit homogeneity. In: Proceedings of the 10th Annual Meeting of ISMRM, Honolulu, 2002. p 903.
30. Vaughan JT, Garwood M, Collins CM, Liu H, DelaBarre, L, Adriany G, Anderson P, Merkle H, Goebel R, Smith MB, Ugurbil K. 7T vs. 4T: RF power, homogeneity, and signal-to-noise comparison in head images. Magn Reson Med 2001;46:24–30.
31. Barfuss H, Fischer H, Hentschel D, Ladebeck R, Oppelt A, Wittig R. *In vivo* magnetic resonance imaging and spectroscopy of humans with a 4T whole-body magnet. NMR Biomed 1990;3:31–45.
32. Adriany G, Heberlein K, Hu X, Andersen P, Ugurbil K, Vaughan JT. Four channel array coil for 4 tesla brain imaging. In: Proceedings of the 10th Annual Meeting of ISMRM, Honolulu, 2002. p 860.
33. Ugurbil K, Garwood M, Ellermann J, Hendrich K, Hinke R, Hu X, Kim S-G, Menon R, Merkle H, Ogawa S. Imaging at high magnetic fields: initial experiences at 4T. Magn Reson Q 1993;9:259–277.